Ion specific tuning of nanoparticle dispersion in an ionic liquid: A structural, thermoelectric and thermo-diffusive investigation

Thiago Fiuza, Mitradeep Sarkar, Jesse Cornelius Riedl, Michel Beaughon, Blanca Torres Bautista, Kakoli Bhattacharya, Fabrice Cousin, Elodie Barruet, Gilles Demouchy, Jerome Depeyrot, et al.

Journal Name

ARTICLE TYPE

Cite this: DOI: 00.0000/xxxxxxxxxx

Ion specific tuning of nanoparticle dispersion in an ionic liquid: A structural, thermoelectric and thermo-diffusive investigation†

T. Fiuza,[a,b] M. Sarkar,[a] J.C. Riedl,[a] M. Beaughon,[c] B.E. Torres Bautista,[c] K. Bhattacharya,[c] F. Cousin,[d] E. Barruet,[e] G. Demouchy,[a,f] J. Depeyrot,[b] E. Dubois,[a] F. Gélébart,[a] V. Gersteen,[e] G. Mériguet,[a] L. Michot,[a] S. Nakamae,[c] R. Perzynski,[a,*] and V. Peyre [a]

Received Date
Accepted Date

DOI: 00.0000/xxxxxxxxxx

Dispersions of charged maghemite nanoparticles (NPs) in EAN (ethylammonium nitrate) a reference Ionic Liquid (IL) are here studied using a number of static and dynamical experimental techniques; Small Angle Scattering (SAS) of X-rays and of neutrons, dynamical light scattering and forced Rayleigh scattering. Particular insight is provided regarding the importance of tuning the ionic species present at the NP /IL interface; In this work we compare the effect of Li^+, Na^+ or Rb^+ ions. The nature of these species has here a clear influence on the short-range spatial organisation of the ions at the interface and thus on the colloidal stability of the dispersions, governing both the NP/NP and NP/IL interactions, which are here both evaluated. The overall NP/NP interaction is either attractive or repulsive. It is characterised by determining, thanks to the SAS techniques, the second virial coefficient A_2, which is found independent of temperature. The NP/IL interaction is featured by the dynamical effective charge ξ_0^{eff} of the NPs and by their entropy of transfer $\hat{S}_{\text{NP}}$ (or equivalently their heat of transport Q^*_{NP}) determined here thanks to thermoelectric and thermodiffusive measurements. For repulsive systems, an activated process rules here the temperature dependence of these two latter quantities.

1 Introduction

Dispersions of magnetic nanoparticles (NPs) in liquids known as Ferrofluids (FF) can be used in numerous applications, as NPs control their magnetic properties while the solvent provides the fluid properties to the FF media[1,2]. These materials flow towards the area where the magnetic field is the strongest. They are used for seals and bearings[1], dampers[3] or in more dilute situations to design optical switches[4], in particular for spatial applications. Using a Room Temperature Ionic Liquid (RTIL) as solvent would allow taking advantage of the thermal stability of this fluid carrier, of its low volatility and, to some extend, of its thermoelectric properties[5–8]. In the literature, colloidal dispersions of magnetic NPs have been obtained in a large number of RTILs[5,6,9–20]. If the importance of the nature of the ions at the NP's interface has been underlined in part of these studies, the systematic tuning of the interface is seldom undertaken[13,15,19,20]. Some elements of rationalisation, proposed from MD simulations on flat interfaces[21], have also been recently considered for the control of the colloidal stability and of the nanostructure of magnetic NP's dispersions in different ionic liquids[19], and as a function of temperature in EMIM TFSI (1-ethyl-3-methylimidazolium bistriflimide)[20]. The aim is now to investigate the influence of this solid/liquid interface on both the static and dynamic properties of the colloidal dispersions in an ionic liquid as a function of temperature. Electrically charged NPs of iron oxide in ethyl ammonium nitrate (EAN) are considered, a system already explored in previous works, appearing quite convenient as a reference system, already explored in previous works[13].

To disperse NPs in ionic liquids, as in all solvents, two interaction forces are of paramount importance; Namely the NP/solvent and the NP/NP interactions. The former controls the dispersibility of the individual NPs (tuning the NP/solvent interaction) while the latter adjusts the dispersion colloidal stability[22]. When electrostatically charged NPs are dispersed in a neat RTIL or in

[a] Sorbonne Université, CNRS, Lab. PHENIX, 4 Place Jussieu, F-75005 Paris, France. Email: regine.perzynski@sorbonne-universite.fr
[b] Grupo de Fluidos Complexos, Inst. de Fisíca, Univ. de Brasília, Brasília (DF), Brazil.
[c] Service de Physique de l'état condensé, SPEC, CEA, CNRS, Université Paris-Saclay, CEA Saclay, 91191 Gif sur Yvette, CEDEX, France.
[d] Lab. Léon Brillouin - UMR 12 CNRS-CEA CEA-Saclay, 91191 Gif-sur-Yvette, France.
[e] Univ. Paris-Saclay, CEA, CNRS, NIMBE - LIONS, 91191 Gif sur Yvette, CEDEX, France.
[f] Univ. de Cergy Pontoise - Dpt de physique, 33 Bd du Port, 95011 Cergy-Pontoise, France.

† Electronic Supplementary Information (ESI) available: [details of any supplementary information available should be included here]. See DOI: 00.0000/00000000.

a concentrated electrolyte, the Debye interparticle electrostatic repulsion - responsible for the stability in polar solvents at low ionic strengths - is fully screened by the highly concentrated ionic atmosphere (up to 11.2 mol.L^{-1} in EAN). However, a re-entrant stability[23] is experimentally observed at high ionic strengths, associated with an anomalous increase of the screening length determined by surface force measurements[24,25], and with a structural self organisation of the concentrated electrolytes[26]. It is this ionic self-organisation around the charged NPs which is usually put forward as being responsible in RTIL for producing the repulsion necessary to counterbalance the van der Waals interparticle attraction (and the magnetic dipolar interaction if - as is the case here - the NPs bear a magnetic moment). This self-organisation can come either from an alternating ionic layering around the NPs[13,19,20,27–29] and/or from solvation forces, associated with hydrogen bonding[15,30].

The chosen system is made of magnetic and charged maghemite nanoparticles in EAN. This protic ionic liquid presents similarities with water, with which it is fully miscible[31]: A pH scale can be defined in EAN[32,33] and a hydrogen bond network exists[34]. The previous studies using the same composition have shown that either citrate-coated NPs[18] or NPs coated with poly(acrylic acid) polyelectrolyte (PAA)[15] can be dispersed in EAN, with different counterions. These works have also evidenced the influence of various parameters: NP structural charge[13], solvation forces sensitive to pH for PAA-coated NPs[15] or NPs size on the colloidal stability of the dispersions at room temperature[35]. When the NP size is too large (typical diameter 11 nm) a liquid-liquid phase separation is observed.

To ensure colloidal stability, we will thus use here small citrate-coated maghemite NPs from a single aqueous batch, with a typical NP diameter of 7.4 nm. These NPs have a net negative charge, around 2 e$^-$ per nm^2 in water, compensated by alkaline monovalent cations; Either lithium Li^+, sodium Na^+ or rubidium Rb^+. Introduced in water before the NP's transfer to EAN, the number of these ions is fixed in the dispersions and corresponds typically to 1% of all the cations for 1 vol% of particles in EAN. Despite this small amount, we show here that these different ions remaining from the aqueous step of the synthesis induce huge modifications to the NP/IL interface.

Specific ion effects are ubiquitous in electrolyte and ionic liquid media, playing a role in areas ranging from battery and supercapacitor efficiency to diverse biological and soft matter mechanisms[36,37]. In aqueous electrolytes, these specific features concern for example the ability to precipitate proteins, first pointed out by Hofmeister[38], or the ability to structure/destructure water via kosmotropic and chaotropic properties[39,40]. In ionic-liquid based media, many ionic specificities have been shown to affect local and global properties, both at interfaces and in bulk materials, namely ionic size and shape, hydrogen-bonding, hydrophobicity, ability to form layers and structures via solvation forces, ...[21,41,42].

We examine here how modifications of the NPs solid interface with EAN, due to different introduced alkaline ions, influence macroscopic effects. The dispersion structure (small angle scattering), thermoelectric and thermodiffusive properties are examined as a function of temperature (T) and NP volume fraction (Φ) for each alkaline ions. The experimental findings are cross-analysed to draw a comprehensive picture of the solid/liquid interface and of both NP/NP and NP/IL interactions.

Section 2 of the paper presents the sample dispersions in EAN and list the various experimental techniques used here to probe the system. The experimental results are then presented and analysed in Section 3, before a final discussion in Section 4. This work illustrates how the NP/solvent interfacial structure directly influences the macroscopic properties of NP dispersions in an Ionic Liquid.

2 Samples and methods

2.1 Sample preparation and composition

The nature of the interface between solid NP's surface and surrounding solvent is a key point in the present study that need to be correlated with the determined properties of the dispersions. The nature and composition of this interface are controlled both in water, where the NPs are synthesised, and through the transfer process to EAN, never drying the NPs as a powder[18].

The NPs are synthesised by a coprecipitation of acidic solutions of $FeCl_2$ and $FeCl_3$ with a strong base, then oxidised in maghemite and dispersed in nitric acid at the end of the process (details in[43,44] and ESI of[45]). The NPs average diameter is 7.4 nm (more details are given in section S1.1 in the ESI. Note that this is the same batch as in Ref.[18]). In a second step citric acid is adsorbed, the nitrate ions are washed and a base XOH is added with the wished counterion that will compensate the citrate once deprotonated, here $X^+ = Li^+$, Na^+ and Rb^+. In all this process, the quantities are controlled as described in the ESI of Ref[45] in order to control the sample composition. The amount of free X_3citrate is fixed at 0.025 mol.L^{-1} and the NPs volume fractions at 1%.

EAN is prepared by acid base reaction as in Refs.[14,18], according to ESI of Ref.[13]. The remaining water content is around 0.3vol% and the pH is around 7-8. It is added to the aqueous dispersions in 50/50 in volume, to obtain EAN/water mixtures. Water is then removed by drying under dynamic vacuum. The initial dispersions in EAN are thus obtained with a NP volume fraction close to 1%, looking stable from visual inspection. Optical microscopy does not reveal any heterogeneity on the micron scale.

In order to obtain samples at higher volume fractions, ultracentrifugation (UC) runs at 250 000g (Optima MAX-XP Ultracentrifuge from Beckman Coulter, 25°C) are performed during 16, 24 or 32 hours. For this sample preparation by UC, all samples are weighted at each step in order to allow checking the mass balance. See ESI Section S1 for more details. Less concentrated samples can then be obtained by diluting with the supernatants obtained from UC. If, at room temperature, monophasic samples at volume fractions as high as $\sim 25\%$ can be obtained with sodium and rubidium counterions, only a volume fraction of $\sim 4\%$ can be reached here for monophasic samples with lithium counterions, because samples phase separate at larger volume fractions[35].

Initial counterion X^+	$[X^+]_{free}$ in EAN mol/L	X^+ coverage /nm^2	Ionic radius R_{ion} (Å)	A_2	D_m (10^{-12} m^{2}s^{-1})
Li^+	0.075 ± 0.001	2.7 ± 0.2	0.6	-6±1	1.2 ± 0.1
Na^+	0.110 ± 0.005	0.6± 0.02	1.02	4.6±0.5	1.2 ± 0.1
Rb^+	0.097 ± 0.010	0.25 ± 0.03	1.64	5.6±1	1.4 ± 0.1

Table 1 For the three studied initial cationic counterions X^+: $[X^+]_{free}$ concentration of free X^+ cations in EAN (not localised on the NPs- see main text) - each value is averaged over 3 supernatants; Surface coverage in term of number of X^+ cations per unit surface of the NPs - Each value is averaged over 4 dispersions with mean NP volume fraction ranging from 1% to 25% (samples monophasic or not - see Section S1.2 of ESI). The provided uncertainty represents the variability over the different samples and does not consider all sources of uncertainty; R_{ion} Ionic radius of these cations[46]; Second virial coefficient A_2, at room T, of monophasic samples as deduced by SAXS (see Section 3.1.1 and Fig. 1-c); Diffusion coefficient D_m from DLS for samples at Φ=1% in dry EAN at room T.

2.2 Chemical determinations of alkali ions

Inductively Coupled Plasma - Mass Spectroscopy (ICP-MS) measurements of lithium, sodium and rubidium content in all samples from UC (i.e., supernatants and dispersions) allow determining the concentration of the free (in supernatant) and total (in dispersions) alkali counterions (see section S1.3 of ESI for experimental details). Considering that the total ion quantity is split between free and bound ions in a given dispersion, we deduce the amount of counterions bound to the nanoparticles in EAN by difference, and convert it into a number of ions per surface unit using the volume fraction of NPs and the specific surface area. The X^+ coverages determined (Table 1) reveal that some alkaline cations stay localised close to the NPs although there is 1 X^+ for around 100 EA^+. The highest adsorption occurs with Li^+ and it is similar to the absorption in water. The remaining free lithium concentration (0.075 mol.L^{-1}) exactly balances the three carboxylates of free citrate in EAN . The X^+ coverage decreases for sodium and even more for rubidium, consistent with the increase of their free concentration, higher than the initial value in water of 0.075 mol.L^{-1}, indicating a release of adsorbed X^+ from the surface in EAN. This is consistent with the trend shown by previous results obtained in samples with lithium and sodium,[35] determined by less efficient Atomic Absorption Spectroscopy.

2.3 Experimental techniques

We explore here the T-range from 22°C to 110°C coupling several techniques. The NP/NP interaction and the resulting colloidal nanostructure are obtained from scattering experiments: Small Angle X-Ray (Swing, Soleil Synchrotron, France) or Neutron (PAXY, LLB, France) Scattering (SAXS/SANS), Dynamic Light Scattering (DLS) and Forced Rayleigh Scattering (FRS) relaxation). For details see sections S2.1 and S3.1 of ESI.

The NP/solvent interaction parameters consists in the effective charge of the moving object ξ_0^{eff} and the Eastman entropy of transfer $\hat{S}_{\text{NP}}$ (defined as Q^*_{NP}/T by Agar et al[47] where Q^*_{NP} is the NP heat of transport[48–50]). They are related to the NP/solvent interfacial properties and are here obtained from the determination of the dispersion properties in thermal gradients, i.e. the induced potential (Seebeck coefficient, thermoelectric effect)[51–53] and the concentration gradient (Soret coefficient, thermodiffusion effect)[48,49,54]. For details see sections S4.1 and S3.1 of ESI.

FRS measurements are also performed under a magnetic field in a concentrated sample ($\Phi \sim 9\%$) with sodium counterions, showing the anisotropy expected in a dispersion of single particles with overall repulsive interaction, thus emphasising stability of such samples.

3 Experimental results and analysis

3.1 Interparticle interaction and structure of the dispersions: influence of the counter-ions

Small angle X-ray and neutron scattering measurements, as well as FRS are performed on the samples with the three counterion types as a function of Φ and T. Let us first mention that, as EAN is hygroscopic*, SAXS measurements have also been performed on samples at 1% of NPs with 5w% of water added to the initial water content of less than ~ 0.3 wt%, in order to estimate its influence. The evolution of I(Q) are similar to the ones without water (See Section S2 and Fig. S2 of ESI), meaning that the presence of 5w% added water does not strongly modify the interactions. The effect of water addition is however revealed by Dynamic Light Scattering experiments, as the associated decrease of viscosity leads to an increase of the diffusion coefficient. Drying under dynamic vacuum enables recovering the sample as before water addition. The diffusion coefficients D_m (after drying under vacuum) and measured at Φ=1% are given in Table 1.

3.1.1 Interparticle interaction at room temperature

The NP/NP interaction is obtained from SAXS measurements on the series of samples obtained by UC for the different counterions, at several volume fractions. Figs 1-a and 1-b present the evolution of the SAXS intensity (normalised by the volume fraction Φ) at room temperature as a function of the scattering vector Q for the obtained dispersions. A comparison with the NP's form factor is also presented. At low Q's and whatever Φ, the normalised intensity for lithium is higher than the form factor, while it is lower for sodium and rubidium. It clearly demonstrates the occurrence of an overall attraction for lithium and an overall repulsion for sodium and rubidium. These results are consistent with the trend seen in samples prepared with NPs from the same batch and sodium or lithium counterions in Ref.[14]. They are also consistent with the smaller range of Φ-stability observed here at

* If for thermoelectric measurements the samples are handled in an atmosphere controlled dry glovebox, they are handled in a less perfectly protected atmosphere for all other experiments.

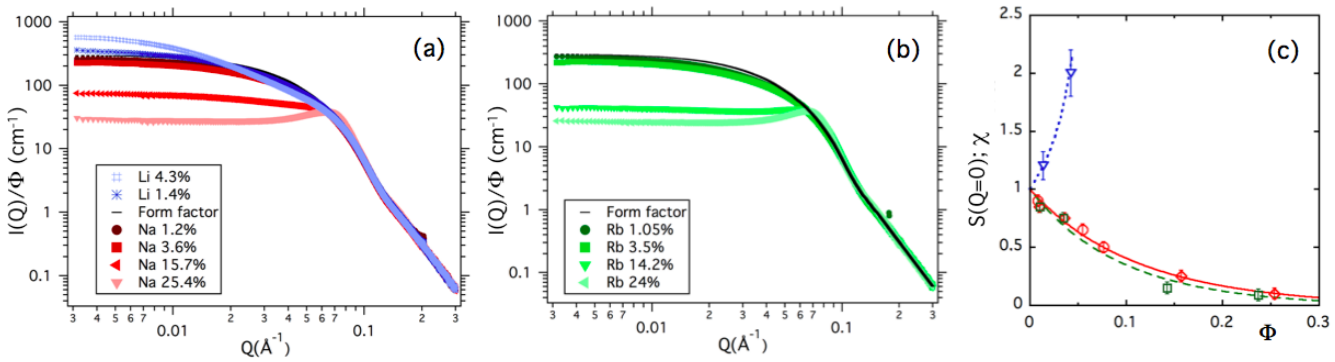

Fig. 1 Small angle X-ray scattering (SAXS) of several dispersions with lithium and sodium counterions (a), rubidium counterions (b),for several volume fractions indicated in the legends (dispersions with Li^+ counterions are not monophasic for $\Phi \geq 4.3\%$). The intensity is normalised by the volume fraction (in %). The reference form factor which corresponds to the pure geometric contribution of the nanoparticles (no interparticle interaction) is plotted on each graph as a full line. (c) Extrapolation at $Q = 0$ of the structure factor $S(Q = 0)$ or compressibility χ of the NP's system as determined by SAXS for EAN-based dispersions for Li^+ counterions (blue open triangles), Na^+ counterions (red circles - Three data point coming from [14] are here added) and Rb^+ counterions (green open squares). Fit of the data for Li^+ (dotted line) is obtained with Eq. 1 and $A_2 = -6$. Fits of the data for Na^+ and Rb^+ are obtained with Eq. S3 of ESI using $\Phi_{eff}/\Phi = 1.15$ for Na^+ (full line: $A_2 = +4.6$) and $\Phi_{eff}/\Phi = 1.4$ for Rb^+ (dashed line: $A_2 = +5.6$).

room temperature for the dispersions with Li^+ counterions than with Na^+ and Rb^+ counterions (see Section 2.1) and Fig. 1.

The corresponding structure factors $S(Q)$ of the various samples can be deduced from these results using Eq. S1 of ESI. Their extrapolation at $Q = 0$ are presented in Figure 1-c as a function of Φ. For repulsive systems (and for dilute enough attractive systems), the quantity $S(Q \to 0)$ is the NP's compressibility χ given by Eq. S2 of ESI.

For low enough volume fractions, the Virial development of the osmotic pressure at the second order links χ with the second order coefficient A_2 as:

$$\chi \sim \frac{1}{1+2A_2\Phi}. \qquad (1)$$

For lithium counterions, a negative value $A_2 = -6 \pm 1$ is extracted from the most dilute sample: χ=1.2 at $\Phi = 1\%$ (at higher Φ's the system is not located in the limit of validity of Eq.1).

For sodium and rubidium counterions, $\chi < 1$, A_2 is positive and the overall interparticle interaction is repulsive. In this case, the compressibility χ strongly decreases with Φ and can no longer be analysed for Φ values typically larger than 1% with Eq.1 .

However it can be described up to large volume fractions (as in Refs.[45,55–58]) by using the Carnahan-Starling development for *effective* hard spheres[59,60] which allows to directly determine A_2. The hard-sphere interparticle potential takes into account the overall interparticle repulsion through a larger NP's radius, which is increased by a characteristic length called l_S by analogy with the screening length used in dilute electrolytes and in concentrated ones with re-entrant stability[24,25]. Assimilating the steep effective hard sphere potential to an exponential decay of characteristic length l_S, the effect of the repulsion would typically extend up to 3 to 5 l_S (see section S.2.2. in ESI for details).

For Na^+ and Rb^+ counterions, the analysis of the compressibilities with Eq. S3 of ESI leads to $A_2 = 4.6 \pm 0.5$ for Na^+ counterions† and 5.6 ± 1 for Rb^+ (see Table1), both values being very close to the Hard Sphere value $A_2 = 4$. Converting A_2 in terms of effective diameter d_{eff} using Eqs. S4 and S5, the obtained characteristic length l_S of the interparticle potential (for $d_{NP} = 7.4$ nm) is small: around 0.2 nm for Na^+ and around 0.4 nm for Rb^+. Such a spatial scale is close to that of the short range force deduced from the colloid probe AFM force-distance measurements between a silica probe and a charged mica plate in EAN of Ref.[61], that was assigned to ionic layering at the interface. It is also very close to the EAN layering near mica surfaces, determined by surface force apparatus in[62].

In summary, at room T, changing the counterions from Na^+ or Rb^+ to Li^+ reverses the interparticle interaction from repulsive to attractive and reduces the range of NPs volume fraction where monophasic stable samples can be obtained, from ~ 25 vol% max with Na^+ or Rb^+, down to ~ 4 vol% max with Li^+ counterions.

3.1.2 Interparticle interaction at high temperatures

The use of thermal gradients on a large range of temperatures raises the question of the structure as a function of temperature. NP/NP interaction is here explored with Small Angle Scattering coupled to DLS for the repulsive NP/NP interaction with Na^+ counterions at Φ = 6.5 %. Figure 2 shows the SANS intensity as a function of the scattering vector Q when the temperature is stationary at 27°C, 60°C, 90°C and back to 27°C. No detectable variation appears, even between the two measurements at 27°C, before and after a long excursion at high T's. The compressibility $\chi = S(Q \to 0)$ of this sample and also its A_2 value are thus at the first order, temperature-independent in the experimental T-range. Such a conclusion is confirmed by the dynamical DLS-measurements done at the same time (see section S.2.3 and Figure S1 of ESI). In the same manner, a static SAXS experiment is performed as a function of temperature for a sample with Li^+

† These results with Na^+ were already published in Bhattacharya et al[18].

counterions at $\Phi = 4.3\%$, presenting NP/NP attractive interaction. At the first order, no T-dependence of the NP/NP interaction is detected (see section S.2.4 and Fig S3 of ESI).

This $T-$independence of the compressibility and thus of the NP/NP interaction in the explored T range is consistent with the low influence of temperature on the short-range structure of EAN studied by AFM experiments at high T's[61]. Note that here, a weak decrease of the short range ordering could be compensated by the weak decrease of dipolar magnetic interaction (attractive on average in zero field)[29].

In summary, it then seems reasonable to extend our conclusion and assume that the compressibility χ and the second virial coefficient A_2 are to the first order, both temperature-independent, for dispersions at any volume fraction for the three counter-ions within the experimental temperature range explored.

3.1.3 Diffusion coefficient

At finite concentration, the diffusion coefficient $D_{\rm m}(\Phi,T)$ depends not only on the friction $\zeta(\Phi,T)$ experienced by the NPs but also on the NP/NP interaction (through the compressibility $\chi(\Phi)$), providing additional information on the nanostructure of the dispersions, *i.e.*:

$$D_{\rm m}(\Phi,T) = \frac{kT}{\zeta(\Phi,T)\chi(\Phi)}. \qquad (2)$$

$D_{\rm m}$ can be determined by relaxation of FRS on a large range of temperature when the gradient of temperature is abruptly put to zero. For more details see section S3.2 of ESI.

Figs. 3 and S4 of ESI present and analyse the diffusion coefficient D_m in zero applied magnetic field for NP dispersions in EAN with the three different counterions at various volume fractions Φ and temperatures T.

At room temperature (Fig. 3-a), whereas for Na^+ and Rb^+, D_m remains almost constant as a function of Φ, up to $\Phi \sim 4\%$, a clear decrease of D_m is observed for Li^+ (in this reduced experimental Φ-range). It suggests that, in this range, the Φ-dependencies of ζ and χ roughly compensate for Na^+ and Rb^+. For Li^+, the decrease of diffusion coefficient results from the increase of both χ and ζ in Eq. 2 (see Fig. 1-c).

When the temperature is increased, the samples with Rb^+ and Na^+ ions, that exhibit overall repulsive NP/NP interaction at room T, remain stable whatever Φ's up to 110°C during the FRS experiment, in good agreement with the weak variation of compressibility with T. On the contrary, the samples with Li^+ counterions, that present overall attractive NP/NP interaction at room T, are not stable from a colloidal point of view (precipitation or phase separation) above $T \sim 80$°C, which was not expected from the SAXS tests. It means that a long stay above 80°C destabilises such samples.

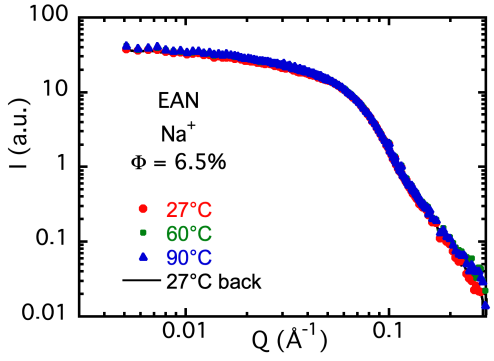

Fig. 2 SANS intensity as a function of the scattering vector at different temperatures T for a sample in EAN at $\Phi = 6.55\%$ with Na^+ counterions

For all these samples, the diffusion coefficient always decreases when T increases. The compressibility χ being known and considered independent on temperature, the friction $\zeta(\Phi,T)$ is determined using Eq. 2. At $\Phi \to 0$ the friction $\zeta_0(T)$ is related to the viscosity $\eta(T)$ experienced by the NPs through:

$$\zeta_0(T) = 3\pi\eta(T)d_H, \qquad (3)$$

d_H being the NP's hydrodynamic diameter. $\eta(T)$ is experimentally obtained at low Φ's using Eqs. S8 and S10 of ESI. This analysis done as a function of T for Na^+ counterions with several samples at Φ's $\sim 1\%$ is presented in Fig. S4-a of ESI. In Eq. S10 of ESI the used hard sphere volume fractions are the values of $\Phi_{\rm eff}$ of Section 3.1.1, with a hydrodynamic diameter $d_{\rm H} = 8.7$ nm, close to the diameter $d_{\rm NP}$. Similar results are obtained with the two other counterions (data not shown). Fig. S4-a of ESI also compares η to $\eta_{\rm EAN}$, the bulk EAN viscosity‡ from literature[63]. We can conclude that at low Φ's, NPs move individually with a hydrodynamic diameter $d_{\rm H} = 8.7$ nm whatever the nature of the counter-ions and feel a viscosity η equal to the bulk viscosity of EAN. These results at low Φ's can also be analysed with an Arrhenius law of an Andrade model[64]. This is shown in Section S3.2 and Figure S4-b in ESI). The activation energy extracted is similar for the three alkaline cations and close to the value for bulk EAN[65,66].

When the volume fraction increases, the friction experienced by the NPs, also increases as shown in Fig.3-b. It displays the friction $\zeta(\Phi,T)$ normalised by $\zeta_0(T)$, as deduced from the experimental values of $D_{\rm m}$ and χ, as a function of Φ for the three families of samples and all available temperatures §. As expected at low Φ's (typically up to $\sim 5\%$) Batchelor's expression[67] (Eq. S10 of ESI) is verified within the experimental error bar whatever the counterion (see Fig. 3-b). At higher Φ's, the friction experienced by the NP's is slightly larger than the phenomenological Dhont's law[68] (Eq. S11 of ESI - see Fig. 3-b for Na^+ and Rb^+).

In conclusion, the diffusion coefficient measurements show that at low Φ's, the NPs move individually, experiencing the bulk EAN viscosity for all T-range explored. They also confirm that the change of the counterion nature reverses the interparticle interaction, affecting also the range of stability of the dispersions. With Na^+ and Rb^+ counterions a superior stability range is observed than with Li^+ in both T and Φ.

‡ Note that $\eta_{\rm EAN}$ is very sensitive to the residual proportion of water in the probed EAN.

§ Still no sample with Li^+ counterions at $\Phi \geq 4\%$ are analysed as these samples are not stable anymore.

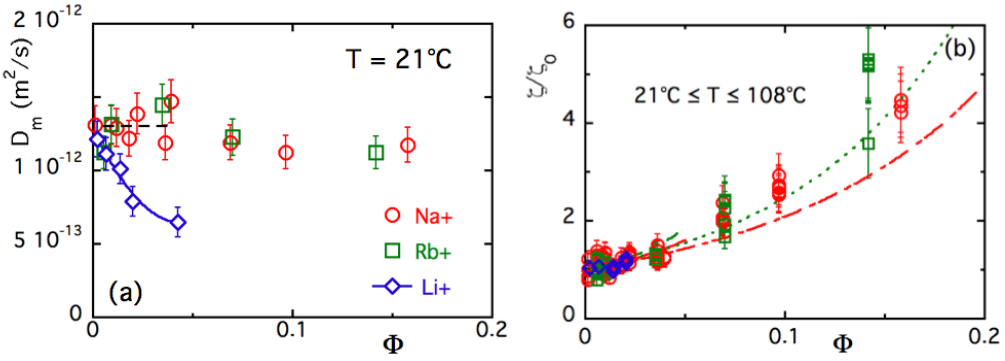

Fig. 3 (a) Evolution of the diffusion D_m of the nanoparticles as a function of their volume fraction Φ at room temperature for the three counterions Li^+, Na^+ and Rb^+; Dashed line corresponds to $D_m = 1.3\ 10^{-12}$ m^2/s; Full line is a polynomial adjustment of Li^+ data, as a guide for the eye; (b) Reduced friction ζ/ζ_0 as a function of Φ for the three counter-ions in the whole range of explored temperatures as deduced from D_m and χ experimental values. For Na^+ (resp. Rb^+) counterions, full (resp. dashed) line corresponds to Eq. S10 up to $\Phi = 5\%$ and dashed/dotted (resp.(dotted) line to Eq. S11, approximating here the hard sphere volume fraction by Φ_{eff} - Same colour of symbols as in Fig.1-c.

3.2 NP/IL interaction : Seebeck and Soret coefficients

The second important interaction corresponds to the affinity of NPs towards the solvent. This can be evaluated with the effective dynamic charge ξ_0^{eff} of the NPs in motion, together with the NP Eastman entropy of transfer $\hat{S}_{NP}$. These two quantities can be determined by coupled thermoelectric (TE) and thermodiffusive (TD) measurements of Seebeck and Soret coefficients.

3.2.1 Initial Seebeck coefficient

As colloidal stability is very similar in NPs dispersions with Na^+ and Rb^+ counterions, we focus here only on one repulsive system with Na^+ counterions and on the attractive one with Li^+ counterions, as they strongly differ. Due to the large TE cell volume, we only probe here samples with volume fraction Φ up to 0.8%.¶ Moreover at higher Φ, the increase of dispersion viscosity reduces the power output. Note that for Li^+, the Seebeck coefficient determination was feasible at $\Phi = 0.3\%$, giving very comparable results to the Na^+ counterparts. At $\Phi = 0.7\%$ stable TE signals could not be obtained.

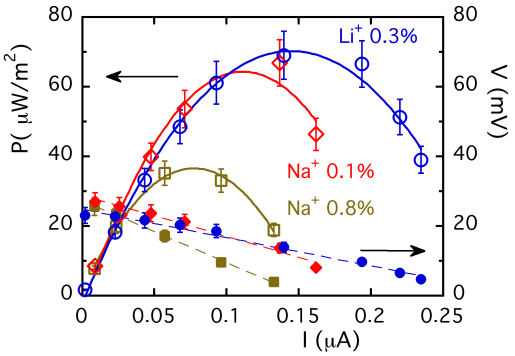

Fig. 4 Thermoelectric voltage V (full symbols) and power per unit surface P (open symbols) as a function of output current for dispersions with either Na^+ or Li^+ counterions at a mean temperature 35°C with electrodes at $T_{cold} = 20$°C and $T_{warm} = 50$°C (heating from the top); Dashed lines are linear fits for $V(I)$ and full lines polynomial fits of the second order for $P(I)$.

¶A redox couple in small quantity is added to the sample to perform the TE measurements (see section S.4.1 of ESI). At low Φ, the colloidal stability is preserved.

We first analyse the thermoelectro-diffusion contribution Se_{TED} to the (initial) Seebeck coefficient $Se = -\Delta V/\Delta T$ measured with the TE-cell before any gradient of concentration is created in the thermocell[52,69]). The experimental variations of Se^{ini}_{TED} as a function of the NP volume fraction Φ for Na^+ and Li^+ counterions are presented in Fig. S9 of ESI at a mean temperature 25°C with electrodes at $T_{cold} = 20$°C and $T_{warm} = 30$°C.

Following Eq. S22 of ESI, the NP contribution $\Delta Se^{ini}_{TED}(\Phi)$ to the initial state Seebeck coefficient Se^{ini}_{TED} can be written as

$$\Delta Se^{ini}_{TED}(\Phi) = t_{NP}(\Phi)\frac{\hat{S}_{NP}}{e\xi_0^{eff}} \quad (4)$$

where $t_{NP}(\Phi)$ is the NP's Hittorf (transport) number, which can be written as $t_{NP} = \sigma_{NP}/\sigma_{tot}$, σ_{NP} being the NP's contribution to the total conductivity σ_{tot} of the dispersion. In the ionic liquid, ξ_0^{eff} cannot be directly measured. However t_{NP} can be experimentally determined, and the ratio $\hat{S}_{NP}/\xi_0^{eff}$ can then be estimated.

As the experimentally determined ΔSe^{ini}_{TED} is positive, the first obvious consequence of this observation is that the ratio $\hat{S}_{NP}/\xi_0^{eff}$ is also positive, i.e. $\hat{S}_{NP}$ and ξ_{eff} being of same sign, and that the values of $\hat{S}_{NP}/\xi_0^{eff}$ are similar for both counter-ion types. As can be seen in Fig. S9 of ESI, the measurement data are rather dispersed, and two extreme attempts are presented for fitting them with Eq.4, using as in Ref.[18] $\sigma_{tot} = 16.22 + 230.86\Phi$ (in mS/cm).

We thus conclude that $\hat{S}_{NP}/\xi_0^{eff} = 0.10\ (\pm 0.05)\ kT\ K^{-1}$ at 25°C.

3.2.2 Power output from the thermoelectric cell

The power output, measured by connecting the electrodes to a variable discharge resistor[52], is a crucial parameter for the use of such liquids in TE applications. both the overall attractive dispersions containing Li^+ and the overall repulsive dispersions containing Na^+ behave in the same way in terms of power output within the range of experimental uncertainties, (see Section S.4.2, Figs. S10 and S11 of ESI). However comparing more closely the mea-

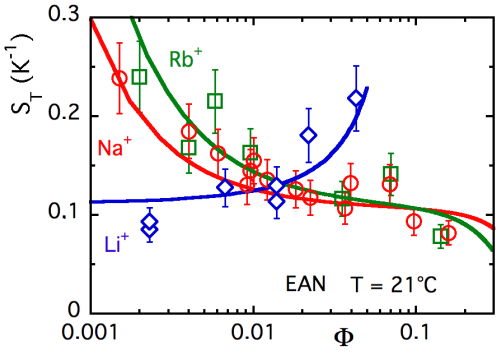

Fig. 5 Soret coefficient S_T as a function of the volume fraction Φ at room temperature for the three counter-ions Na^+, Rb^+ and Li^+ - same symbols as in Fig.1-c; The full lines correspond to the adjustements of $S_{T(\Phi)}$ for the three counter-ions with the formalism of Section 3.2.4.

surements at the same NP volume fraction, with the same T_{cold} / T_{warm} combination, a clear influence of the nature of the NP/IL interface can be evidenced. In Fig. 4, at $\Phi \sim 0.3\%$, the power output per unit surface P is roughly 50% larger for dispersions with Li^+ counterions than for Na^+ ones. It can thus be concluded that tuning the NP/IL interface is indeed a relevant tool in TE developments. ||.

3.2.3 Soret coefficient in zero magnetic field: $S_T(\Phi,T)$ measurements

The Soret coefficient S_T can be determined from Forced Rayleigh scattering experiments (see details in Section S3.1 of ESI), in stationary conditions of the concentration gradient under temperature gradients. Indeed in the presence of both $\vec{\nabla}T$ and $\vec{\nabla}\Phi$, the flux $\vec{j}_\Phi$ of NPs is:

$$\vec{j}_\Phi = -D_m(\Phi,T)(\vec{\nabla}\Phi + \Phi S_T \vec{\nabla}T). \quad (5)$$

In stationary conditions, $\vec{j}_\Phi = \vec{0}$ leading to the expression of Soret coefficient S_T given by Eq. S6 of ESI and the fluxes $\vec{j}_i$ of all the other ionic species are nul as well. According to Refs.[18,51,55,56] and disreagarding in a first approximation the negligible term $\frac{1}{\Phi}\frac{\partial \Pi V_{NP}}{kT}\frac{\partial}{\partial T}$ in the model, S_T can be written as:

$$S_T = \chi\left(\frac{\hat{S}_{NP}}{kT} - e\xi_0^{eff}\frac{S_e^{st}}{kT}\right) \quad (6)$$

where e is the elementary charge and S_e^{st} is the stationary Seebeck coefficient associated to the internal field $\vec{E}^{st} = -S_e^{st}\vec{\nabla}T$ in the conditions of the FRS experiment.

The room-temperature evolutions with NP's volume fraction Φ of S_T are displayed in Fig.5 for the three counterions. Whatever the counterion nature, the Soret coefficient is positive, meaning that NPs present a thermophobic behavior (if $\vec{\nabla}T$ is positive along a reference axis, $\vec{\nabla}\Phi$ is negative along this same axis in Eq. S6 of ESI). This figure also shows that, for each of the three counterions Li^+, Na^+, and Rb^+, there is a direct correlation between the Φ-dependence of S_T (Fig 5) and that of χ (Fig.1-c), which increase/decrease in the same way.

|| Note however, that whatever the nature of the counterions, the presence of NPs decreases the electrical power collected from the thermo-cell. This reference system, that is interesting from a scientific point of view, is therefore not suitable for thermoelectric applications.

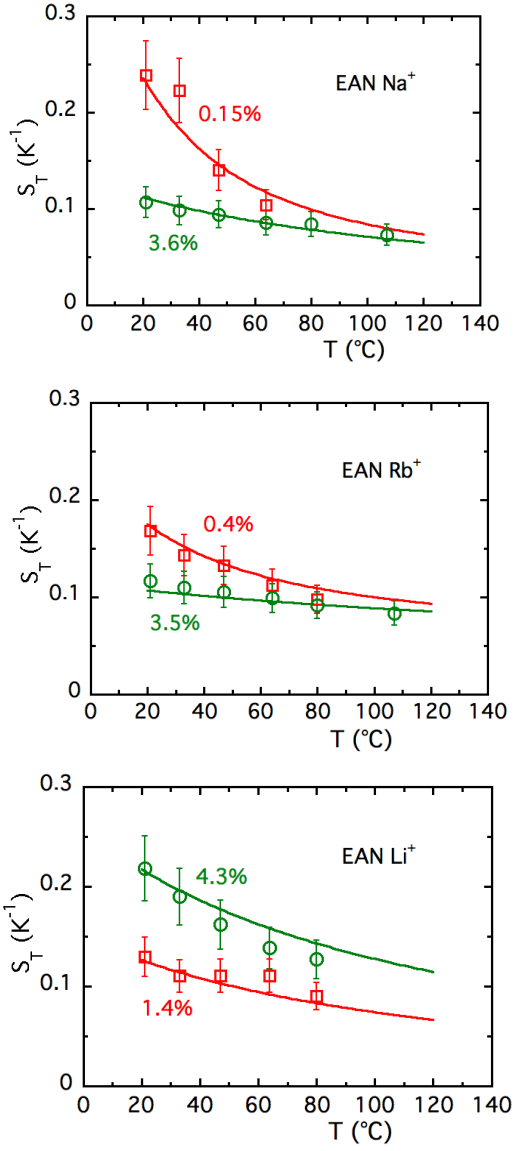

Fig. 6 Soret coefficient S_T as a function of T at different Φ's for the three counterions; The full lines correspond to the adjustments of $S_T(T)$ with the formalism of Sections 3.2.4.

Let us now focus on the temperature dependence of S_T in zero magnetic field. It is presented in Fig.6 for the three different counterions, in the FRS accessible range of volume fraction Φ (up to 14% for Na^+ and Rb^+; up to 4.2% for Li^+) and temperatures T (up to 110 °C for Na^+ and Rb^+; up to 80 °C for Li^+). Whatever the counterion, volume fraction and temperature, the Soret coefficient S_T is here positive and is a decreasing function of T in the whole FRS experimental range.

Initial counterion	ξ_0^{eff}	$\frac{\hat{S}_{\text{NP}}}{kT}$ (K^{-1})	$\frac{\hat{S}_{\text{NP}}}{kT}/\xi_0^{\text{eff}}$ (K^{-1})	n_+ (mole.L^{-1})	Q^*_{NP} (eV)
Na^+	55 ± 15	6.0 ± 1.6	~ 0.11	$4\ (\pm\ 1).\ 10^{-4}$	45 ± 9
Rb^+	30 ± 8	3.3 ± 1.0	~ 0.11	$4\ (\pm\ 1).\ 10^{-4}$	25 ± 5
Li^+	~ 1	0.11 ± 0.03	~ 0.11	$2\ (\pm\ 0.5).\ 10^{-3}$	0.7 ± 0.2

Table 2 Room-temperature NP's parameters for the fits of Fig.5: ξ_0^{eff} dynamic effective charge, $\hat{S}_{\text{NP}}$ Eastman entropy of transfer, n_+ number of dissociated ionic species of positive charge, $Q^*_{\text{NP}} = T\hat{S}_{\text{NP}}$ heat of transport

3.2.4 Soret coefficient in zero magnetic field: $S_{\text{T}}(\Phi, T)$ analysis

The determined Soret coefficients versus T and Φ are analysed with a formalism initially proposed for NP dispersions in polar solvents[51,55,56]. In Eq. 6, the stationary Seebeck coefficient S_e^{st} (Eq. S11 of ESI) is obtained writing electro-neutrality of the system and assimilating (as in Refs.[18,55,56]) trivalent citrate ions to three monovalent CH_3COO^-. Providing approximations detailed in Section S3.4 of ESI, S_{T} can be written as:

$$S_{\text{T}} = \chi \frac{\hat{S}_{\text{NP}}}{kT} \left(\frac{2n_i + n_{\text{NP}}\ |Z_0^{\text{eff}}|}{2n_i + n_{\text{NP}}\ |Z_0^{\text{eff}}|\ (1 + \chi\ |\xi_0^{\text{eff}}|)} \right). \qquad (7)$$

where $n_{\text{NP}} = 6\Phi/(\pi d_{\text{NP}}^3)$ and n_i are respectively the number per unit volume of NPs and of dissociated ionic species of the same sign as NPs. Z_0^{eff} is the NP's static effective charge (see Section 3.4 of ESI) which is of the same order of magnitude as the NP's dynamic effective charge ξ_0^{eff}. As in[18,56,70], they are assimilated to each other in the following fits.

Eq.7 shows that $\hat{S}_{\text{NP}}$ has the same sign as S_{T}. $\hat{S}_{\text{NP}}$ is thus here positive, whatever the counter-ion and whatever T. Moreover, as the Seebeck measurements evidence that $\hat{S}_{\text{NP}}$ and ξ_0^{eff} have the same sign (see Section 3.2.1), the effective charge of the NPs is here necessarily positive. In Eq.7, $|Z_0^{\text{eff}}|$ and $|\xi_0^{\text{eff}}|$ can be replaced respectively by Z_0^{eff} and ξ_0^{eff} and n_i by n_+.

Fig. 5 displays the best fits at room T for the three alkaline ions at the NP/IL interface, using the parameters listed in Table 2. A huge difference of properties of the solid/liquid interface between the two dispersions with overall interparticle repulsion (Na^+ and Rb^+ ions) and the dispersions with overall interparticle attraction (Li^+ ions) can clearly be observed. More details on the adjustments on the whole Φ range are given in Section S3.5 of ESI and, for some limiting cases, in Section S3.6 of ESI.

The same fitting procedure can be applied to S_{T} at higher T. Fig. 6 shows these fits as a function of T while Fig. S7 of ESI shows the fits as a function of Φ for different T. Keeping n_+ (Table 2) small and constant, the NP/IL interaction parameters ξ_{eff} and $\hat{S}_{\text{NP}}$ are found to depend strongly on T for Na^+ and Rb^+ counterions, while they remain unaffected for Li^+. This will be discussed with more details in Section 4.2.2.

In summary, S_{T} strongly depends on NP/NP and NP/IL interactions, dictated by the nature of the counterions, for the whole explored T range.

3.2.5 In-field anisotropy of S_{T} and D_{m} at room temperature

The under-field stability of the colloidal dispersion and the anisotropy of D_{m} and S_{T}, are here probed at room temperature with a sample with Na^+ counterions at $\Phi = 9.3\%$. The mixture also contains a few % of water (~ 5 weight%), which could slightly reduce the colloidal stability. If this small amount of water has little influence on the $S_{\text{T}}(H = 0)$ value obtained in zero field ($= 0.12\ \text{K}^{-1}$), the situation is markedly different for the diffusion coefficient $D_{\text{m}}(H = 0)$ ($= 2.1 \times\ 10^{-12}\ \text{m}^2\text{s}^{-1}$), that is significantly higher than the values deduced from Fig.3-a ($= 1 \times\ 10^{-12}\ \text{m}^2\text{s}^{-1}$); This is due to the presence of water that decreases the viscosity of the fluid carrier by a factor of the order of 2.

Nevertheless Fig. S5 of ESI shows that this sample is stable at least up to an applied magnetic field H of 100 kA/m, and presents a reversible behaviour when going back to zero field after the high field measurements. Moreover, the under-field anisotropy is well described by the model extensively described in Refs.[29,53,56].

It can be therefore concluded that the samples are very stable under magnetic field and have anisotropic properties, S_{T} changing by a factor here around 2 between the directions parallel and perpendicular to the magnetic field. The magnetic field can thus be considered as a tuning parameter for thermoelectric properties[69].

4 Discussion

It is shown in this work that the nature of the counterions present at the NPs interface in water during the initial stage of the synthesis has a strong influence on the physical properties of the NP dispersions in EAN. These ions partly remain close to the NP in the ionic liquid, changing both the NP/NP interaction and the NP/IL interaction. They consequently modify the nanostructure of the dispersions and the NP thermophoretic properties as well as the TE, however less affected. Let us see if we can understand how the ionic interface can be organised in the ionic liquid.

4.1 Ion specificity of the ionic layering around the NPs

Many studies on interfaces between neat ionic liquids and solids, insulating or conducting but mainly with flat surfaces, have revealed the presence of layered ionic structures parallel to the interface[27,71]. More recently some organisation inside the first and second layers close to the solid surface were also evidenced[21,72] and simulated[73,74]. The details depend on the RTIL's nature, that of the surface, and on the surface charge, as well as on the additives. On NPs which are curved and rougher than the flat models[27,71], the organisation is expected to be perturbed and similar experiments looking directly at the structure of the interface are not feasible. Nevertheless, all knowledge acquired on flat surfaces remains very informative.

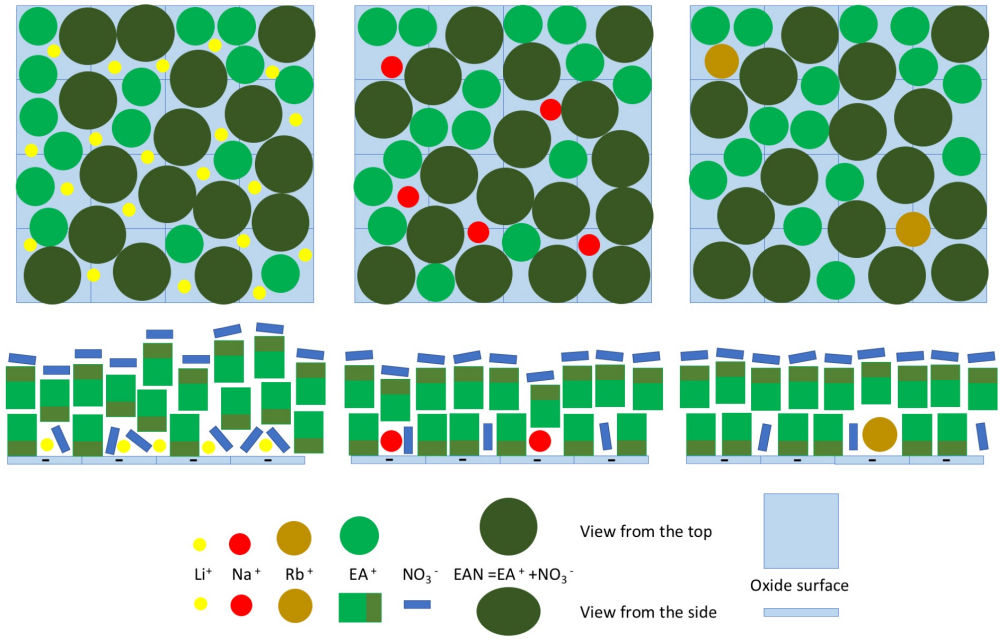

Fig. 7 Tentative sketch of the local ionic organisation close to the NP's interface in EAN RTIL, in the three different situation considered here, taking into account the measured number of adsorbed X^+ ions and geometrical considerations: (left) with counterions Li^+, (right) with counterions Rb^+ and (in between) with counterions Na^+; (top) View of the first ionic layer, from above the surface, (bottom) legend with the various symbols, (middle) lateral view of the first two layers.

In water, at neutral pH and low ionic strength, the iron oxide NPs used here are negatively charged thanks to a layer of adsorbed citrate ions, leading to a structural charge Z_{str} of 32 μC/cm^2 (around 2 elementary charges per nm^2) [75] corresponding to Z_{str}= - 315 for one NP here. This high charge is compensated by X^+ counterions, here Li^+, Na^+ or Rb^+, that constitute a Stern layer of ions bound on the surface and a diffuse layer at larger distances. Given the size of these cations compared with the charge density on the surface, this first layer is mainly composed of water, in addition to these bound ions. The static effective charge Z_{eff} as well as the dynamic one ξ_o^{eff} determined from electrophoresis is much smaller than Z_{str} and close to -20 [56]. It is the effective charge (both static and dynamic) associated with the diffuse ionic layer around the NP, which is responsible for the NP/NP electrostatic repulsion in aqueous colloids.

When the NPs are transferred to EAN, the citrate ions bound to the NP surface remain while the free citrate species dissolve in the surrounding EAN, X_3Citrate salts being soluble in EAN. The elementary charge to compensate at the solid/liquid interface is thus still 2 per nm^2. Note that this value is close to that of mica surfaces, used in a standard way for many studies of IL organisation close to a surface by AFM or Surface Force Apparatus (SFA), which are thus reasonably comparable to our situation. The surface charge can be compensated only by ions, here EA^+ or X^+ cations. However in the IL there is no neutral individual species available to fill the remaining volume as in water. There are only ions (EA^+ and nitrate anions NO_3^-, that could form pairs). This raises the question of the ionic organisation of ILs close to the solid interface.

In most of the studied combinations solid/IL, a 2D-like structure is formed close to the solid interface with a structuring perpendicular to the interface and a possible organisation parallel to the interface, which forms a transition towards the 3D organisation of the bulk IL [72,76]. In the case of EAN, the bulk structure can be considered as a sponge-like structure with polar and apolar domains gathering the small ethyl chains [77]. In the vicinity of a negative surface this sponge-like structure of EAN becomes lamellar. The bulk sponge structure is recovered above few layers, as seen experimentally for instance by SFA [62,78] or AFM [79]. The thickness of the detected layers is around 0.5 nm, close to the size of an EAN pair [62], however composition and organisation of the layers remain unknown.

Based on geometrical considerations, we can estimate the ratio κ_{ion} of the solid surface charge density to the charge density that the EA^+ counterions can produce with maximum packing, ratio that has been shown to be relevant in MD simulations to link the surface layering and the geometry of the ions [21]. The ammonium head of EA^+ is taken to be 3.6 Å and should then occupy an area of 13 Å^2 on the surface, which can produce a maximal charge of 123 μC/cm^2 for a full layer. Comparing to 32 μC/cm^2 of the NP solid surface, it is geometrically possible to add 4 EA^+ per surface charge, which corresponds to $\kappa_{ion} \simeq 0.25$. According to various MD simulations, such a ratio is not optimal to maximise the organisation of the IL at the interface, as maximal layering is expected for κ_{ion}= 0.5. It further suggests that the first layer mixes cations and anions, as already seen in other systems [80].

In the colloidal dispersions considered here, chemical determination (see Table 1) proves that the X^+ cations have more affinity

towards the surface than towards the bulk. Their amount on the solid surface increases while cation diameter decreases, which points to an electrostatic interaction with the surface. Given the size of the cations, a lot of surface remains available for other species in the first layer, that can be filled by EA^+ cations and NO_3^- anions of EAN pairs. Fig. 7 is a tentative sketch showing how to construct the first layer between the X^+ cations with the available species, EAN, and EA^+. The size of an EAN pair is around 5.5 Å[76,77] and the distance between EA^+ cations can be estimated to be 3.6 Å[77]. With these values, the X:EA ratio in the first layer can be obtained for the 3 cations for two extreme hypotheses: only EAN pairs or only EA^+ cations filling the first layer. This yields 1:1 to 1:2.5 for Li^+, 1:5 to 1:12 for Na^+ and 1:13 to 1:30 for Rb^+. Fig. 7 proposes an intermediate situation. Whatever the hypothesis, the interface is modified compared with pure EAN, due to the size mismatch between X^+ and EAN, especially large for lithium cations.

In pure EAN, where the only possible counterions are the EA^+ ions, studied in Refs.[14,35], interparticle interaction strength falls between the cases of Li^+ and Na^+ counterions (see Section S6 of ESI). Partly replacing EA^+ by sodium or rubidium increases interparticle repulsion through a better organisation at the interface. The result is especially surprising for Rb^+ which yields the strongest repulsion although its amount at the interface is low compared to EA^+. It also reveals that even a small change in the ionic population at the interface can have a huge impact on the dispersions' nanostructure and physical properties. For these dispersions with Na^+ and Rb^+, the range of the produced repulsion is short (0.6-2 nm), as determined from SAXS in Section 3.1.1. Such a value is compatible with the layering of EAN, known to form layers of the order of 0.5 nm close to a surface[62].

On the contrary, partly replacing EA^+ by Li^+ reduces the layering effect needed for ensuring interparticle repulsion leading to colloidal stability. This can be due to the structure breaking character of lithium ions in EAN[81]. The repulsion is then not high enough for overcoming the van der Waals attraction and the magnetic dipolar interaction, that is on average attractive. This results in a weak global attractive NP/NP interaction. Destabilisation while heating is observed only with lithium counterions, that may be due to a weakening of the layering with temperature as observed for EAN on mica[79] where the force to disrupt a layer decreases with temperature as well as the number of layers.

These results are consistent with some recent experiments where more Li^+ or Na^+ ions are added in either the Li^+- or Na^+-based dispersions studied here[82]. More Li^+ or Na^+ ions are then found close to the NPs, evidencing an equilibrium between free and linked species. Moreover, Li^+ tends to replace Na^+, in agreement with its high affinity for the NPs surface.

In summary, these results provide a good static image of the solid/liquid interface with a first layer different from the following ones, as shown on Figure 7, with a quite different local ionic organisation in the case of Na^+ and Rb^+ adsorbed counterions (associated to a regular ionic layering) and in the case of Li^+ (with less organised first ionic layers).

4.2 Ion specificity and NP/IL interaction parameters

The dynamical behaviour is another important question and governs the effective charge ξ_0^{eff} involved when NPs are moving under an applied force, as shown here in thermodiffusion and thermoelectric measurements. It depends on the charge of the solid body of the NP, the composition of the first layer and the position of the shear plane in the layered structure close to the interface. The first layer can compensate or overcompensate the structural charge Z_{str} of NPs. The apparent charge on this layer can thus here be negative as the surface of the NP, null or even reversed, thus positive. The surface experiments show that this first layer is very difficult to remove from the surface[78,79] and that the second layer also can be strongly modified by additives. Consequently, the NPs should move at least with this first layer of highly bound species (as the Stern layer in water), which defines a shear plane location where ξ_0^{eff} is defined. Other layers may move with the particle and this can be modified by the presence of the alkaline cations. Therefore values of ξ_0^{eff} with a modulus between 0 and $|Z_{str}|$ or even slightly larger are possible. From these considerations, we then argue that ξ_0^{eff} can take values between 0 and ± 350 to fit the data, Z_{str} being chosen as a good order of magnitude of the maximum possible ξ_0^{eff}.

4.2.1 NP/IL interaction parameters at room T

The combined analysis of thermoelectric and thermodiffusive measurements lead to positive values of ξ_0^{eff} at room T (see Table 2 and section 3.2.4), which may correspond to NPs moving with the first ionic layer overcompensating the negative NP structural charge. The values however strongly depend on the composition of the NPs interface.

For Na^+ and Rb^+ counterions, both ξ_0^{eff} and $\hat{S}_{\text{NP}}$ are rather large in EAN at room temperature with respect to standard values in water[55,56]. The NP's heat of transport $Q^*_{\text{NP}} = T\hat{S}_{\text{NP}}$ at room temperature (Table 2) is then also large and of the same order of magnitude as those found in DMSO for acid NPs[51], namely $Q^*_{\text{NP}} \sim 20$ eV at room T. They are coherent with the electrostatic nature of the NP/IL interaction. In water, due to H-bond links, negative values of Q^*_{NP} and $\hat{S}_{\text{NP}}$ are often found (but not always)[55,56,83,84]. This is consistent with a good organisation around the NPs, which is sufficient to produce an overall repulsive interparticle interaction.

By opposition, for Li^+ counterions, both ξ_0^{eff} and $\hat{S}_{\text{NP}}$ are found much smaller at room temperature than with Na^+ and Rb^+. The values of $\hat{S}_{\text{NP}}/kT$ and Q^*_{NP} (see Table 2) for Li^+ are here close to those found for citrate-coated NPs in water with bulky hydrophobic $TBuA^+$ counterions[45,56,85]. This is consistent with a poor ionic organisation around the NPs, which is not sufficient to produce an overall repulsive interparticle interaction.

4.2.2 NP/IL interaction parameters as a function of T

The T-dependence of the NP/IL interface is extracted from the fits of S_{T} as a function of T (Figures 6 and S7 of ESI), which give the evolution of ξ_0^{eff} and $\hat{S}_{\text{NP}}$ with T (see Figs. 8 and 9).

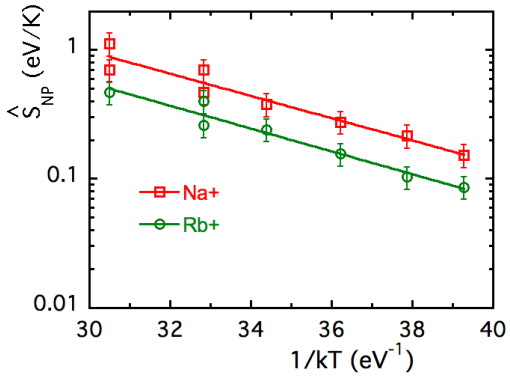

Fig. 8 Eastman entropy of transfer $\hat{S}_{NP}$ of the nanoparticles as a function of $1/kT$ for Na^+ and Rb^+ counterions as deduced from the adjustments of $S_T(\Phi,T)$ of Sections 3.2.4 and 4.2.2; Full lines are the best fits of the values by the Arrhenius law of Eq. 8.

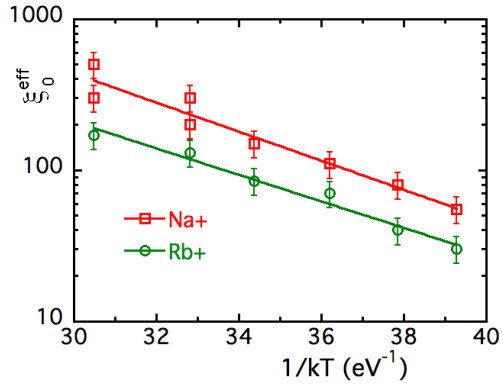

Fig. 9 Effective charge ξ_0^{eff} of the nanoparticles as a function of $1/kT$ for Na^+ and Rb^+ counterions as deduced from the adjustments of $S_T(\Phi,T)$ of Sections 3.2.4 and 4.2.2; Full lines are the best fits of the values by the Arrhenius law of Eq. 8.

For Na^+ and Rb^+ counterions, the ratio $\hat{S}_{NP}/\xi_0^{eff}$ is almost constant and independent on the counterion, in agreement with the initial Seebeck measurements of Section 3.2.1. Both ξ_0^{eff} and $\hat{S}_{NP}$ increase with T following an Arrhenius law of the form

$$\hat{S}_{NP} \propto \xi_0^{eff} \propto exp^{-Ea/kT} \quad (8)$$

with an activation energy $Ea = 0.20 \pm 0.02$ eV. This value is extremely close to that observed for pure EAN by NMR determinations of the temperature dependence of the diffusion coefficient of translation of both EA^+ and NO_3^- ions by Filippov et al[65] (see Section S5 and Fig. S12 of ESI). A similar value $Ea = 0.22$ eV (21.75 kJ/mol) is obtained from viscosity measurements of EAN by Zarrougui et al[66].

For Li^+ counterions, the effective charge ξ_0^{eff} at room T is rather small (of the order of 1) for the entire T-range explored. Therefore Eq. 7 can be simplified in Eq. S18 (see ESI for more details) and $\hat{S}_{NP} = kTS_T/\chi$. The determined $\hat{S}_{NP}$ is almost independent on T (see Section S7 and Fig. S13 of ESI), which means that TS_T is almost constant, as χ does not depend on T at first order.

In addition to the huge difference in the T-dependence of ξ_0^{eff} and $\hat{S}_{NP}$ for the different interfaces, their values also differ by around two orders of magnitude. For Li^+, ξ_0^{eff} is around 1 and $\hat{S}_{NP}$ is of the order of 2.5 meV/K ($\sim 4\ 10^{-22}$ J/K as at room T), both being independent on T. On the contrary, for Na^+ and Rb^+, $\hat{S}_{NP}$ varies typically from ~ 0.1 eV/K ($\sim 1.6\ 10^{-20}$ J/K) at room temperature up to ~ 1 eV/K ($\sim 1.6\ 10^{-19}$ J/K) at 108°C. On the same T-range, ξ_0^{eff} varies from several tens up to several hundreds (i.e. up to the NP's structural charge at the highest T).

In summary, the similar weak decrease of the Soret coefficient S_T with T is related to highly different interfacial phenomena depending on the interface composition and results from a subtle balance between the two terms $\hat{S}_{NP}/kT$ and $-e\xi_0^{eff}S_e^{st}/kT$ in Eq. 6 that can differ by orders of magnitude depending on the NP/IL interface.

5 Conclusions

We have shown the impact of ion specificity on the ionic liquid organisation around the NPs. This organisation controls to a large extent the overall NP/NP interaction, that can be repulsive on average even at high T's. With well chosen counterions, here Na^+ and Rb^+, highly stable fluid samples at high NP volume fraction can be produced, remaining stable under a strong applied magnetic field and over a wide temperature range. On the contrary, as small Li^+ cations are structure breaking in EAN, their presence at the NP/IL interface disturbs the organisation in layers at the NP interface. This leads to a much smaller Eastman entropy of transfer $\hat{S}_{NP}$ for the dispersed NPs and to overall attractive NP/NP interaction. In such conditions, the colloidal stability of the dispersion is achievable on a smaller range of volume fraction ($\Phi \leq 4.3\%$) and near room temperature.

It is shown that Soret coefficient measurements at different volume fractions smaller than 1% allow discriminating here between a positive or repulsive overall balance of interparticle interaction in the dispersion. When the interparticle interaction balance is repulsive, it can be described with a Carnahan-Starling formalism of effective hard spheres. Then, both the effective charge ξ_{eff} and the Eastman entropy of transfer $\hat{S}_{NP}$ present a thermally activated behaviour, ruled by an activation energy which is very close to that of pure EAN. It is fully compatible with the diffusion coefficient measurements at low Φ's showing that the effective viscosity experienced by the NPs while thermally diffusing, is that of the EAN carrier fluid.

This work demonstrates that the choice of the surface species on the nanoparticles is crucial (even when these species are minority ones) for designing a NP dispersion in an RTIL and tuning its properties, especially for their scale-up production intended for high temperature applications.

Author Contributions

Dr Thiago Fiuza : PhD student in Physics shared between PHENIX - Sorbonne Univ. (SU) - France and GCF - Univ. de Brasilia (UnB) - Brazil, under the co-direction of Pr J. Depeyrot - UnB and Pr R. Perzynski - SU. He defended his PhD in December 2020. In-

volved in the SAXS and SANS measurements and their analysis, he performed and analysed optical measurements with the forced Rayleigh scattering device.

Dr Mitradeep Sarkar: Post-doctoral fellow appointed by EU program H2020 MAGENTA in PHENIX-SU, under the supervision of Dr G. Demouchy and Pr R. Perzynski. He developed the software of the forced Rayleigh scattering device, performed measurements on the colloidal dispersions with T. Fiuza and took part in the global analysis.

Dr Jesse C. Riedl: PhD student in Physical-Chemistry appointed by EU program H2020 MAGENTA in PHENIX-SU under the co-direction of Dr E. Dubois and Dr V. Peyre, he defended his PhD in September 2020. He synthesised the colloidal dispersions in the ionic liquid and characterised them by numerous techniques, in particular, their stability by SAXS and SANS, with T. Fiuza.

Dr Michel Beaughon: PhD student in Physics under the direction of Dr Sawako Nakamae in SPEC - CEA - Univ. Paris Saclay. He defended his PhD in December 2021. He was involved in the TE measurements and associated to data analysis.

Dr Bianca E. Torres Bautida: Post-doctoral fellow appointed by EU program H2020 MAGENTA in SPEC-CEA Saclay under the supervision of Dr Sawako Nakamae. She was in charge of thermoelectric and electrochemical measurements and characterisations.

Dr Kakoli Bhattacharya: Post-doctoral fellow appointed by EU program H2020 MAGENTA in SPEC-CEA Saclay under the supervision of Dr Sawako Nakamae. She was in charge of thermoelectric measurements.

Mrs Elodie Barruet: Technician at LIONS - CEA - Univ. Paris-Saclay. She made the ICP-MS determinations with V. Gersteen.

Dr Fabrice Cousin: Researcher at C.E.A. and Member of Lab. Léon Brillouin, responsible for the SANS device. He was piloting SANS measurements and participating to SAXS measurements. He has been deeply involved in the experimental analysis of the results.

Dr Gilles Demouchy: Assistant-Professor at Cergy-Pontoise Univ. - France and member of PHENIX-SU, co-responsible for the post-doc of M. Sarkar. Optical measurements on the forced Rayleigh scattering device have been performed under his supervision.

Pr. Jérome Depeyrot: Professor at Universidade de Brasilia and member of GCF-UnB, co-director of the PhD thesis of T. Fiuza, has coordinated his work on the colloidal dispersions in ionic liquids and the analysis of his experimental results.

Dr Emmanuelle Dubois: Director of Research at CNRS and member of PHENIX-SU, co-director of the PhD work of J. C. Riedl. She has largely contributed to the synthesis of the samples and to the analysis and interpretation of the measurements, in particular for their physico-chemical aspects.

Mr Frédéric Gélébart: Engineer at CNRS and member PHENIX-SU. He has developed the automatic set-up for sample thermalization and magnetic field application in the forced Rayleigh scattering device.

Dr Valérie Gersteen: Researcher at LIONS - CEA - Univ. Paris-Saclay. She made the ICP-MS determinations with E. Barruet.

Pr Guillaume Mériguet: Professor at Sorbonne Université and member of PHENIX-SU. He has been involved in the development of the forced Rayleigh scattering device, the development of the models and the analysis of the results.

Dr Laurent Michot: Director of Research at CNRS and director of PHENIX-SU. He was deeply involved in the measurements and analysis of SAXS determinations in Soleil - Gif sur Yvette.

Dr Sawako Nakamae: Researcher at SPEC - CEA Saclay, director of the PhD thesis of M. Beaughon and responsible for the post-doc of B. E. Torres Bautida. She is in charge of the development of all the experimental aspects of thermoelectricity in magnetic colloids in SPEC - CEA Saclay

Pr Régine Perzynski: Professor at Sorbonne Université and member of PHENIX-SU, co-director of the PhD thesis of T. Fiuza and co-responsible for the post-doc of M. Sarkar. She has coordinated their work, in particular for the global analysis and the confrontation with the models.

Dr Véronique Peyre: Assistant-Professor at Sorbonne Université and member of PHENIX-SU, co-director of the PhD work of J. C. Riedl. She has been deeply involved in the synthesis and characterisation of the dispersions of magnetic nanoparticles in the ionic liquid, in particular for the physico-chemical aspects.

Conflicts of interest

There are no conflicts to declare.

Acknowledgements

We acknowledge synchrotron SOLEIL (France) for the X-ray beam-time allocation on the SWING spectrometer and the support of J. Perez during the experiments. We thank also the Laboratoire Léon Brillouin, CEA-Saclay, France for the neutron beam-time allocation at PAXY spectrometer and especially Arnaud Hélary for technical assistance with the SANS-DLS setup. This research was supported by ANR TEFLIC (grant number ANR-12-PRGE-0011-01), LabEx PALM (ANR-10-LABX-0039-PALM), the European Union's Horizon 2020 research and innovation programme under the grant agreement n° 731976 (MAGENTA) and the bilateral programs CAPES- COFECUB Ph 959/20 (between France and Brazil). We also acknowledge the funding from the Brazilian agencies FAP/ DF and CNPq thanks to contract PRONEX-FAPDF (2017-2021) 0193.001194/2016, the financial support of CNPq (through the Grant 202009/2018-1 & the contract INCT-FCx grant 2014/ 50983-3) and FAP-DF (Grant 0193.001376/2016).

Notes and references

1 R. Rosensweig, *R. Rosensweig*, Cambridge University Press, Cambridge, 1985.

2 E. Blums, A. Cēbers and M. Maiorov, *Magnetic Liquids*, W. de G. Gruyter, New York, 1997.

3 *Ferrofluids : Magnetically Controllable Fluids and Their Applications*, ed. S. Odenbach, Springer Verlag, Berlin, 2003.

4 J. Philip and J. Kaskar, *J. of Nanofluids*, 2012, **1**, 3–20.

5 Z. He and P. Alexandridis, *Adv. Colloid Interface Sci.*, 2017, **244**, 54–70.

6 X. Shi, W. Huang and X. Wang, *Lubr. Sci.*, 2018, **30**, 73–82.

7 T. Okabe, Y. Kondo, S. Yoshimoto and S. Sasaki, *Vacuum*, 2019, **164**, 30–40.

8 M. Dupont, D. MacFarlane and J. Pringle, *Chem. Commun.*, 2017, **53**, 6288–6302.

9 F. C. C. Oliveira, L. M. Rossi, R. F. Jardim and J. C. Rubim, *The J. Phys. Chem. C*, 2009, **113**, 8566–8572.

10 L. Rodríguez-Arco, M. T. López-López, F. González-Caballero and J. D. Durán, *J. Colloid Interface Sci.*, 2011, **357**, 252–254.

11 N. Jain, X. Zhang, B. S. Hawkett and G. G. Warr, *ACS Appl. Mater. Interfaces*, 2011, **3**, 662–667.

12 A. Mederios, A. Parize, V. Oliveira, B. Neto, A. Bakuzis, M. Sousa, L. Rossi and J. Rubim, *ACS Appl. Mater. Interfaces*, 2012, **4**, 5458–5465.

13 M. Mamusa, J. Siriex-Plénet, F. Cousin, E. Dubois and V. Peyre, *Soft Matter*, 2013, **10**, 1097–1101.

14 M. Mamusa, J. Sirieix-Plénet, F. Cousin, R. Perzynski, E. Dubois and V. Peyre, *J. Phys.: Condens. Matter*, 2014, **26**, 284113.

15 C. Guibert, V. Dupuis, J. Fresnais and V. Peyre, *J. Colloid Interface Sci.*, 2015, **453**, 105–111.

16 L. Mestrom, *Nanotechnology*, 2015, **26**, 285602.

17 P. Priyananda, H. Sabouri, N. Jain and B. Hawkett, *Langmuir*, 2018, **34**, 3068–3075.

18 K. Bhattacharya, M. Sarkar, T. J. Salez, S. Nakamae, G. Demouchy, F. Cousin, E. Dubois, L. Michot, R. Perzynski and V. Peyre, *ChemEngineering*, 2020, **4**, 5 1–25.

19 J. C. Riedl, M. A. Akhavan Kazemi, F. Cousin, E. Dubois, S. Fantini, S. Loïs, R. Perzynski and V. Peyre, *Nanoscale Adv.*, 2020, **2**, 1560–1572.

20 J. C. Riedl, M. Sarkar, T. Fiuza, F. Cousin, J. Depeyrot, E. Dubois, G. Mériguet, R. Perzynski and V. Peyre, *J. Colloid Interface Sci.*, 2022, **607**, 584–594.

21 V. Ivaništšev, S. O'Connor and M. Fedorov, *Electrochem. Commun.*, 2014, **48**, 61–64.

22 J. Gao, R. S. Ndong, M. B. Shiflett and N. J. Wagner, *ACS Nano*, 2015, **9**, 3243–3253.

23 H. Yuan, W. Deng, X. Zhu, G. Liu and V. Craig, *Langmuir*, 2022, **38**, 6164–6173.

24 A. Smith, A. A. Lee and S. Perkin, *J. Phys. Chem. Lett.*, 2016, **7**, 2157–2163.

25 A. A. Lee, C. Perez-Martinez, A. Smith and S. Perkin, *Phys. Rev. Lett.*, 2017, **119**, 026002 1–5.

26 T. Groves, C. Perez-Martinez, R. Lhermerout and S. Perkin, *J. Phys. Chem. Lett.*, 2021, **12**, 1702–1707.

27 M. Mezger, H. Schröder, H. Reichert, S. Schramm, J. S. Okasinski, S. Schöder, V. Honkimäki, M. Deutsch, B. M. Ocko, J. Ralston, M. Rohwerder, M. Stratmann and H. Dosch, *Science*, 2008, **322**, 424–428.

28 V. Kamysbayev, V. Srivastava, N. B. Ludwig, O. J. Borkiewicz, H. Zhang, J. Ilavsky, B. Lee, K. W. Chapman, S. Vaikuntanathan and D. V. Talapin, *ACS Nano*, 2019, **13**, 5760–5770.

29 T. Fiuza, M. Sarkar, J. C. Riedl, A. Cēbers, F. Cousin, G. Demouchy, J. Depeyrot, E. Dubois, F. Gélébart, G. Mériguet, R. Perzynski and V. Peyre, *Soft Matter*, 2021, **17**, 4566–4577.

30 J. Gao, P. Mwasame and N. Wagner, *J. Rheol.*, 2017, **61**, 525–535.

31 D. Takacs, M. Tomsic and I. Szilagyi, *Colloids Interfaces*, 2022, **6**, 2–14.

32 N. Benlhima, D. Lemordant and P. Letellier, *J. Chim. Phys.*, 1989, **86**, 1919–1939.

33 R. Kanzaki, K. Uchida, S. Hara, Y. Umebayashi, S.-I. Ishiguro and S. Nomura, *Chem. Lett.*, 2007, **36**, 684–685.

34 K. Fumino, A. Wulf and R. Ludwig, *Angew. Chem. Int. Ed.*, 2009, **48**, 3184–3186.

35 M. Mamusa, J. Sirieix-Plénet, R. Perzynski, F. Cousin, E. Dubois and V. Peyre, *Faraday Discuss.*, 2015, **181**, 193–209.

36 R. Miranda-Quintana and J. Smiatek, *J. Phys. Chem. B*, 2021, **125**, 13840–13949.

37 K. Gregory, G. Elliott, H. Robertson, A. Kumar, E. Wanless, G. Webber, V. Craig, G. Andersson and A. Page, *Phys. Chem. Chem. Phys.*, 2022, **24**, 12682–12718.

38 F. Hofmeister, *Naunyn- Schmiedeberg's Arch. Pharmacol.*, 1888, **25**, 1–30.

39 G. Jones and M. Dole, *J. Am. Chem. Soc.*, 1929, **51**, 2950–2964.

40 Y. Marcus, *Chem. Rev.*, 2009, **109**, 1346–1370.

41 H. Zhao, *J. Chem. Technol. Biotechnol.*, 2016, **91**, 25–50.

42 D. Diddens, V. Lesch, A. Heuer and J. Smiatek, *Phys. Chem. Chem. Phys.*, 2017, **19**, 2043020440.

43 R. Massart, *C. R. Acad. Sci. Paris*, 1980, **291**, 1–3.

44 R. Massart, *I.E.E.E., Trans. on Magn.*, 1981, **2**, 1247–1248.

45 C. L. Filomeno, M. Kouyaté, V. Peyre, G. Demouchy, A. Campos, R. Perzynski, F. A. Tourinho and E. Dubois, *J. Phys. Chem. C*, 2017, **121**, 5539–5550.

46 J. Mähler and I. Persson, *Inorg. Chem.*, 2012, **51**, 425–438.

47 J. Agar, C. Mou and J. Lin, *J. Phys. Chem.*, 1989, **93**, 2079–2082.

48 A. Majee and A. Würger, *Phys. Rev. E*, 2011, **83**, 061403.

49 K. A. Eslahian, A. Majee, M. Maskos and A. Würger, *Soft Matter*, 2014, **10**, 1931–1936.

50 A. Würger, *Phys. Rev. Lett.*, 2021, **126**, 068001 1–5.

51 B. Huang, M. Roger, M. Bonetti, T. J. Salez, C. Wiertel-Gasquet, E. Dubois, R. C. Gomes, G. Demouchy, G. Mériguet, V. Peyre, M. Kouyaté, C. L. Filomeno, J. Depeyrot, F. A. Tourinho, R. Perzynski and S. Nakamae, *J. Chem. Phys.*, 2015, **143**, 054902.

52 T. J. Salez, B. T. Huang, M. Rietjens, M. Bonetti, C. Wiertel-Gasquet, M. Roger, C. L. Filomeno, E. Dubois, R. Perzynski and S. Nakamae, *Phys. Chem. Chem. Phys.*, 2017, **19**, 9409–9416.

53 T. Salez, S. Nakamae, R. Perzynski, G. Mériguet, A. Cēbers and M. Roger, *Entropy*, 2018, **20**, 405.

54 A. Würger, *Phys. Rev. Lett.*, 2008, **101**, 108302.

55 R. Cabreira-Gomes, A. da Silva, M. Kouyaté, G. Demouchy, G. Mériguet, R. Aquino, E. Dubois, S. Nakamae, M. Roger, J. Depeyrot and R. Perzynski, *Phys. Chem. Chem. Phys.*, 2018, **20**, 16402–16413.

56 M. Kouyaté, C. Filomeno, G. Demouchy, G. Mériguet, S. Naka-

mae, V. Peyre, M. Roger, A. Cēbers, J. Depeyrot, E. Dubois and R. Perzynski, *Phys. Chem. Chem. Phys.*, 2019, **21**, 1895–1903.
57 E. Wandersman, A. Cebers, E. Dubois, G. Mériguet, A. Robert and R. Perzynski, *Soft Matter*, 2013, **9**, 11480.
58 C. Filomeno, M. Kouyaté, F. Cousin, G. Demouchy, E. Dubois, L. Michot, G. Mériguet, R. Perzynski, V. Peyre, J. Sirieix-Plénet and F. Tourinho, *J. Magn. Magn. Mat.*, 2017, **431**, 2–7.
59 N. Carnahan and K. Starling, *J. Chem. Phys.*, 1970, **53**, 600.
60 J. A. Barker and D. Henderson, *J. Chem. Phys.*, 1967, **47**, 4714–4721.
61 N. Hjalmarsson, R. Atkin and M. Rutland, *Chem. Commun.*, 2017, **53**, 647–650.
62 Y. Fung and S. Perkin, *Faraday Discussion*, **- to appear in 2023**,.
63 J. Smith, G. Webber, G. Warr and R. Atkin, *J. Phys. Chem. B*, 2013, **117**, 13930–13935.
64 E. da C. Andrade, *Nature*, 1930, **125**, 309–310.
65 A. Filippov, O. Gnezdilov, N. Hjalmarsson, O. Antzutkin, S. Glavatskih, I. Furo and M. Rutland, *Phys. Chem. Chem. Phys.*, 2017, **19**, 25853–25858.
66 R. Zarrougui, M. Dhahbi and D. Lemordant, *J. Solution Chem.*, 2015, **44**, 686–702.
67 G. K. Batchelor, *J. Fluid Mech.*, 1982, **119**, 379–408.
68 J. K. G. Dhont, *An Introduction to Dynamics of Colloids*, Elsevier Science, 1996, pp. 1–642.
69 T. Salez, M. Kouyaté, C. L. Filomeno, M. Bonetti, M. Roger, G. Demouchy, E. Dubois, R. Perzynski, A. Cēbers and S. Nakamae, *Nanoscale Adv.*, 2019, **1**, 2979–2989.
70 M. Sarkar, J. C. Riedl, G. Demouchy, F. Gélébart, G. Mériguet, V. Peyre, E. Dubois and R. Perzynski, *Eur. Phys. J. E*, 2019, **42**, 979–2989.
71 R. Hayes, N. Borisenko, M. Tam, P. Howlett, F. Endres and R. Atkin, *J. Phys. Chem. C*, 2011, **115**, 6855–6863.
72 A. Elbourne, M. Dupont, R. Kariuki, N. Meftahi, T. Daeneke, T. L. Greaves, C. F. McConville, G. Bryant, S. J. Bryant, Q. A. Besford and A. J. Christofferson, *Advanced Materials Interfaces*, 2023, **2202110**, 1–14.
73 S. D. Lecce, A. A. Kornyshev, M. Urbakh and F. Bresme, *Phys. Chem. Chem. Phys.*, 2021, **23**, 22174–22183.
74 S. Kondrat, G. Feng, F. Bresme, M. Urbakh and A. A. Kornyshev, *Chemical Rev.*, **to appear in 2023**,.
75 E. Dubois, V. Cabuil, F. Boué and R. Perzynski, *J. Chem. Phys.*, 1999, **111**, 7147–7160.
76 J. Segura, A. Elbourne, E. Wanless, G. Warr, K. Voïtchovsky and R. Atkin, *Phys. Chem. Chem. Phys.*, 2013, **15**, 3320.
77 R. Hayes, S. Imberti, G. G. Warr and R. Atkin, *Phys. Chem. Chem. Phys.*, 2011, **13**, 3237–3247.
78 R. G. Horn, D. F. Evans and B. W. Ninham, *J. Phys. Chem.*, 1988, **92**, 3531–3537.
79 R. Hayes, G. G. Warr and R. Atkin, *Phys. Chem. Chem. Phys.*, 2010, **12**, 1709–1723.
80 A. Elbourne, S. McDonald, K. Voïchovsky, F. Endres, G. G. Warr and R. Atkin, *ACS Nano*, 2015, **9**, 7608–7620.
81 R. Hayes, S. A. Bernard, S. Imberti, G. G. Warr and R. Atkin, *J. Phys. Chem. C*, 2014, **118**, 21215–21225.
82 C. Guibert and V. Peyre, *private communication*.
83 S. Alves, G. Demouchy, A. Bée, D. Talbot, A. Bourdon and A. M. Figueiredo Neto, *Philosophical Magazine*, 2003, **83**, 2059–2066.
84 A. Sehnem, A. Figueiredo Neto, R. Aquino, A. Campos, F. Tourinho and J. Depeyrot, *Phys. Rev. E*, 2015, **92**, 042311 1–8.
85 C. Filomeno, T. Fiuza, M. Kouyaté, J. Riedl, M. Sarkar, G. Demouchy, J. Depeyrot, E. Dubois, G. Mériguet, R. Perzynski and V. Peyre, *Chapter 5 in Material Aspects of Ferrofluids*, CRC Press, Taylor & Francis Group, R.P. Pant - 2023 edn, 2023, pp. 94–115.